

Table of Contents

S-1 DNP at 1.2 T / 34 GHz / 13 MHz.....	2
S-1.1 Instrumentation and sample preparation.....	2
S-1.2 Determination of the saturation factor by ELDOR.....	2
S-1.3 DNP signal build-up (T_{BuildUp}) and nuclear relaxation time ($T_{1,n}$).....	4
S-1.4 Microwave irradiation for DNP experiments.....	5
S-1.5 Evaluation of DNP enhancements.....	6
S-1.6 Summary of ^{13}C -DNP parameters.....	7
S-1.6.1 $^{13}\text{CCl}_4$ + TN.....	7
S-1.6.2 $^{13}\text{CCl}_4$ + FN2a.....	8
S-1.6.3 $^{13}\text{CHCl}_3$ + TN.....	10
S-1.6.4 $^{13}\text{CHCl}_3$ + FN2a.....	11
S-1.6.5 Diethyl malonate-2- ^{13}C + TN.....	11
S-2 DNP at 9.4 T / 263 GHz / 100 MHz.....	13
S-2.1 Instrumentation and sample preparation.....	13
S-2.2 MW saturation and temperature effect.....	14
S-2.3 ^{13}C -NMR enhancements.....	15
S-2.4 ^{13}C -NMR line width under DNP conditions.....	16
S-2.5 EPR spectra at 263 GHz.....	17
S-2.6 Spin count and NMR sensitivity.....	17
S-3 DNP at 14 T / 395 GHz / 150 MHz.....	19
S-4 Mechanistic model for the coupling factor.....	21
S-4.1 Influence of temperature on the coupling factor at high fields.....	24
S-5 DFT calculations of ^{13}C hyperfine coupling.....	25
S-6 References.....	28

S-1 DNP at 1.2 T / 34 GHz / 13 MHz

S-1.1 Instrumentation and sample preparation

EPR/DNP experiments at 1.2 Tesla were performed using a Bruker ElexSys E580 EPR spectrometer and a Bruker AVANCE III ^1H 400 MHz NMR console. A Bruker cylindrical resonator ER-5106QT/W capable of storing sample tubes up to 3 mm outer diameter was used. To detect NMR signals, a copper coil (< 3 mm outer diameter, 1.6 mm inner diameter) was inserted into the resonator. For $^{13}\text{CCl}_4$, ^{13}C -NMR detection of thermal equilibrium signals was possible with ~ 100 scans. The electromagnet was constructed for EPR experiments and does not provide shimming and locking capabilities.

The Bruker microwave (MW) bridge was equipped with a 3 W MW amplifier capable of pulse and CW irradiation for both EPR and DNP measurements. The MW excitation field B_1 was measured by Rabi nutation in deuterated BDPA dispersed in polystyrene matrix, being $B_1 \sim 0.6$ MHz. A decrease of this value is expected in liquid samples due to dielectric losses. To increase DNP performance we used a 40 W TWT CW amplifier (IFI – Instruments For Industry). However, due to elevated noise figure and the absence of gating, the device was not suitable for EPR measurements.

For all experiments at 1.2, 9.4 and 14 T samples were prepared from the same materials: $^{13}\text{CCl}_4$ and $^{13}\text{CHCl}_3$ (Cambridge Isotope Laboratories Inc.), nitroxide radical (TN, ^{15}N and d_{16} labeled) (Isotech), $^{13}\text{CBr}_4$ and ^{13}C labeled organic molecules (Aldrich Chemistry). Spin counting calibration for setting the proper radical concentration was performed via CW EPR at X band / 0.34 T on a Bruker Elexys E500 instrument.

For experiments at 1.2 T, samples were inserted into EPR quartz tubes (inner diameter 0.8 mm, outer diameter 1.6 mm) and degassed by freeze–pump–thaw cycles (two to four) to remove O_2 and consequently increase MW saturation. Sample volumes were 8 – 10 μL .

S-1.2 Determination of the saturation factor by ELDOR

Saturation factors at 34 GHz were measured by electron-electron double resonance experiments (Türke 2011) (ELDOR, inset of Figure S1b). On the ELDOR channel, a saturation pulse (3 – 5 μs) was applied to reach a steady state condition ($T_{1,e} < 1 \mu\text{s}$). The ELDOR spectrum was recorded as a function of the frequency of this pulse. The typical sweep range of 100 – 130 MHz was chosen in order to cover the EPR spectrum of the nitroxide radical, which shows two (in case of ^{15}N) or three (in case of ^{14}N) EPR lines separated by ~ 60 MHz or 43 MHz, respectively (Figure S1a). A $\pi/2$ detection pulse is applied on resonance either with the low field or the high field line. The integrated free induction decay (FID) is recorded as a function of the ELDOR frequency (Figure S1b). A signal reduction is recorded when the ELDOR pulse is on or close to resonance with one of the EPR lines. Consequently, with s_1 and s_2 measured as the normalized signal drops in the case of a two-line spectrum, the effective saturation factor s can be obtained as follows:

$$s = s_{\text{eff}} = (s_1 + s_2) / 2$$

The efficiency of ELDOR for measuring saturation factors was previously demonstrated for ^{15}N -nitroxide radicals (Türke 2011). For TN at Q band the ELDOR effect is symmetric when pumping either on the low or the high field line. For the fullerene nitroxide FN2a, the ELDOR experiment could be performed only by detecting on the low field line. As the EPR line is not symmetric around the center (Figure S2) and in DNP only the low field line is pumped, the validity of an ELDOR with detection on the low field line was tested. EPR FID intensities were monitored on each of the line as a function of the pumping pulse length, when the latter was on resonance with the low field line, as for DNP experiments (Figure S2). The two saturation values were then compared and turned out to be similar within the error (Figure S8).

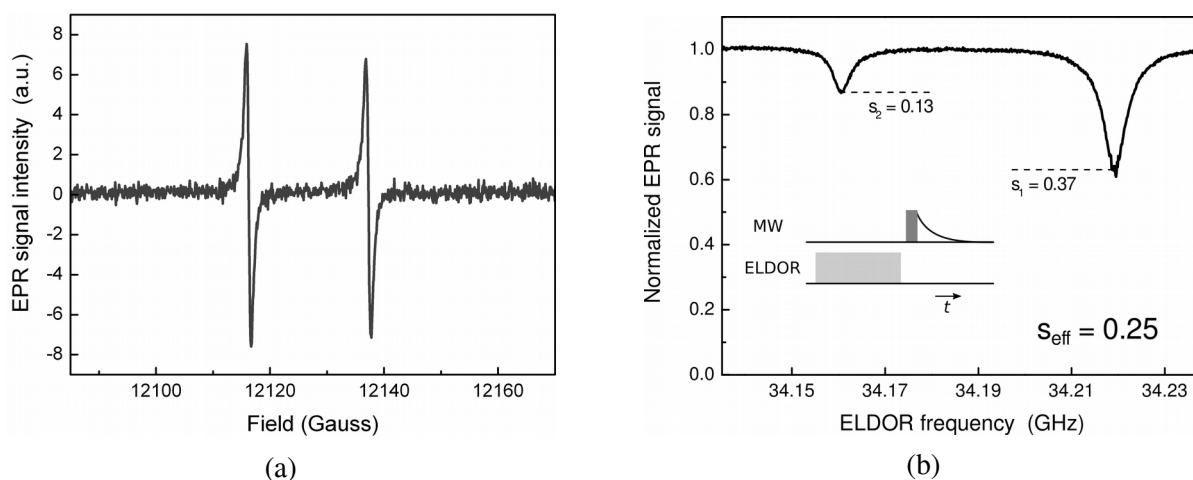


Figure S1. EPR spectrum and ELDOR saturation experiment. (a) CW EPR spectrum at 34 GHz of TN radical in CHCl_3 (10 mM). The splitting of ~ 21 G corresponds to a hyperfine splitting of ~ 60 MHz. (b) ELDOR trace obtained in CHCl_3 doped with TN at 10 mM is shown here as an example. The ELDOR sequence is in the inset.

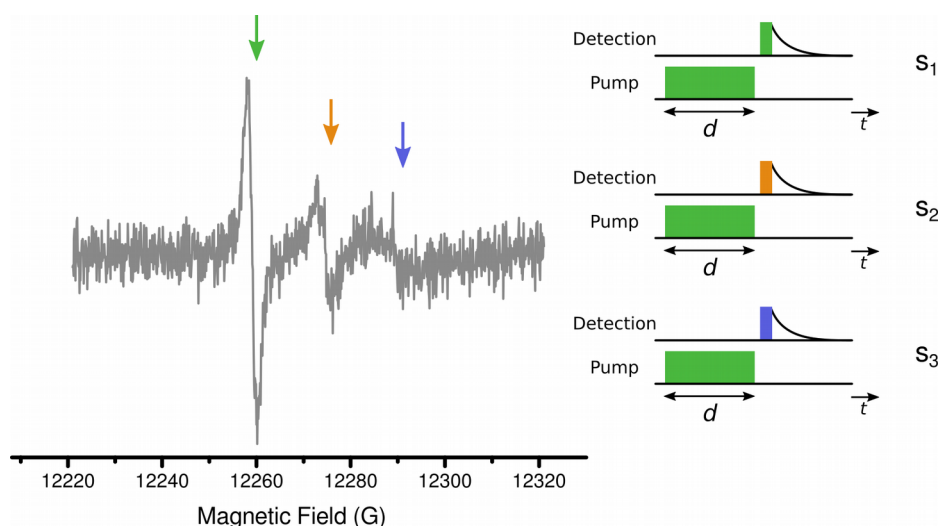


Figure S2. Pump-detection scheme for saturation measurements for FN2a. CW-EPR spectrum at 34 GHz of fullerene nitroxide in CCl_4 is shown. The saturation factor is measured by recording FID intensity of each line as a function of the pump pulse length, as displayed on the right. The pumping was on resonance with the low field line, as for DNP experiments. The color code defines the frequencies of the three lines. The effective saturation for the three lines case is calculated as $(s_1 + s_2 + s_3)/3$.

The theoretical expression for s_1 and s_2 was previously derived for ^{15}N nitroxide radical (Türke 2012):

$$s_1 = 1 - \frac{w_e(2(w_e + w_n) + \omega_{ex})}{0.25 \gamma_e^2 B_1^2 T_{2,e}(4w_e + 2w_n + \omega_{ex}) + w_e(2(w_e + w_n) + \omega_{ex})} \quad (\text{S1})$$

$$\frac{s_2}{s_1} = 1 - \frac{2}{2 + \frac{w_n}{w_e} + \frac{\omega_{ex}}{2w_e}} \quad (\text{S2})$$

where B_1 is the MW excitation field, $2w_e = 1/T_{1,e}$ the electron spin-lattice relaxation rate, ω_{ex} the Heisenberg exchange rate, w_n the ^{15}N spin-lattice relaxation rate, and $T_{2,e}$ the longitudinal relaxation time. The Heisenberg exchange rate is defined as $\omega_{ex} = C \cdot K_x$, where C is the polarising agent concentration and K_x is the exchange coupling constant. For nitroxide radical, $K_x = 2.5 \pm 0.8 \times 10^9 \text{ s}^{-1} \text{ M}^{-1}$ (Liu 2017).

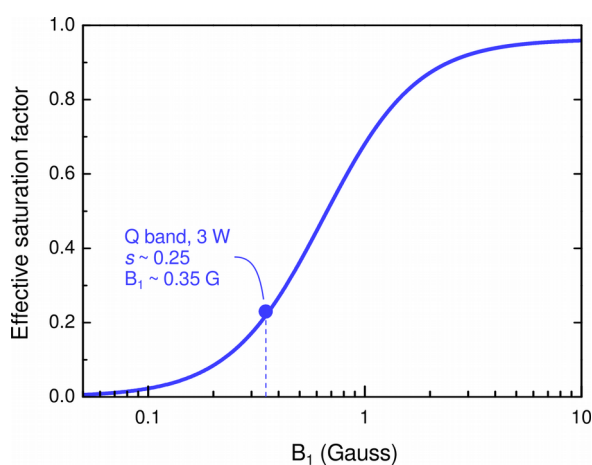


Figure S3. Dependence of the effective saturation on the MW excitation field. Effective saturation curve is calculated with Equations S1 and S2 for TN in CCl_4 (20 mM) at 1.2 T (Q band) with the following parameters: $B_1 = 0.35 \text{ G}$, $T_{1,e} = 500 \text{ ns}$, $T_{2,e} = 30 \text{ ns}$, $K_x = 2.5 \times 10^9 \text{ s}^{-1} \text{ M}^{-1}$. The circle marks the value measured in our DNP setup at 1.2 T. Experimental saturation values (Section S-1.6.1 and Figure S6) are in good agreement with the predicted ones.

S-1.3 DNP signal build-up (T_{buildUp}) and nuclear relaxation time ($T_{1,n}$)

By comparing T_{BuildUp} and $T_{1,n}$ one can estimate the temperature effect on the sample under DNP conditions (Türke 2012b). For this goal, DNP build-up curves were obtained by measuring the NMR signal intensity as a function of the MW irradiation pulse length. The data were then fitted with the exponential function $I = A \cdot [1 - \exp(-t/T_{\text{BuildUp}})]$. An example, together with the pulse sequence, is shown in Figure S4a.

The nuclear relaxation time $T_{1,n}$ was recorded under DNP conditions after a MW pumping pulse. The pulse length was calibrated in order to observe an enhanced signal and, at the same time, kept as short as possible to limit changes of the sample temperature. The DNP decay curve was fitted by the exponential function $I = A \cdot \exp(-t/T_{1,n})$. Figure S4b shows a fitted decay and the pulse sequence used.

We concluded that for CCl_4 and CHCl_3 heating of the sample under MW irradiation was negligible since $T_{\text{BuildUp}} \sim T_{1,n}$ (Table S1-S4). This was further confirmed by measurements of the cavity quality factor, as illustrated in the next section.

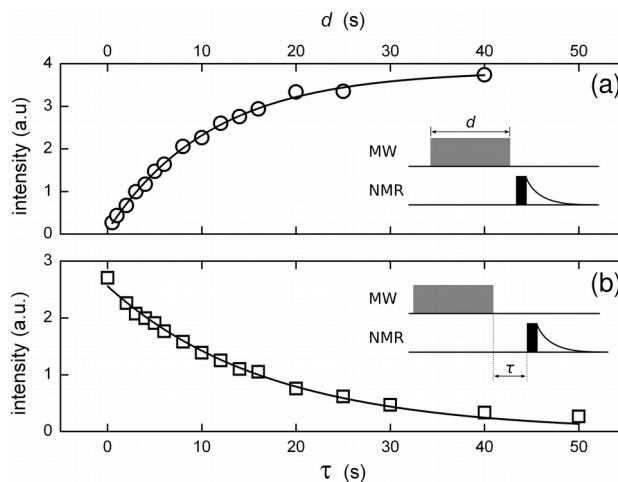


Figure S4. Nuclear relaxation experiments. Examples of (a) build-up and (b) $T_{1,n}$ relaxation curves obtained for $^{13}\text{CCl}_4$ doped with TN (10 mM) at 1.2 T (13 MHz for ^{13}C). The sequences are shown in the insets.

S-1.4 Microwave irradiation for DNP experiments

DNP experiments require MW pulses with duration of $\sim 5 \cdot T_1$. For ^{13}C this corresponds to MW irradiation times in the range 1 s – 120 s. Due to software limitation, pulses longer than a few milliseconds were not achievable. Therefore, a quasi-CW pulse was obtained with a pulse train having 100 μs pulse-length and 1 μs separation, as depicted in Figure S5.

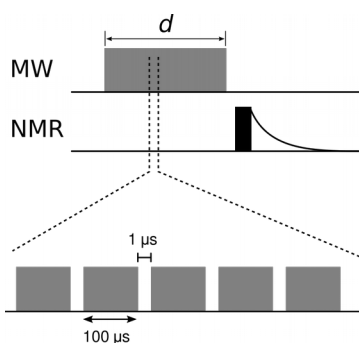


Figure S5. DNP pulse sequence. MW and rf pulses are displayed as a function of time. d is the total duration of the MW irradiation. The quasi-CW scheme obtained with a pulse train is shown as well.

In a first set of experiments, a 3 W microwave amplifier was used to record the DNP enhancement under the same conditions as in the ELDOR experiments. Power output was checked with a power meter in the two conditions (i.e. quasi-CW operation and 5 μs ELDOR pulse). A slight power loss ($< 5\%$) during quasi-CW

operations (1 - 120s) was observed. However, this deviation is not significant and was considered within the experimental error.

In a second set of experiments, a 40 W TWT amplifier was used to maximize the NMR enhancements. Due to hardware limitations (Section S-1.1) that did not allow for EPR detection, saturation measurements under these conditions were not possible.

For long irradiation times in CW operation, a deviation of the cavity resonance position might occur due to eddy currents and consequent heating of the cavity (Türke 2010). This effect could alter the performance of the cavity during DNP experiments. Furthermore, the variation in full-width half-maximum (FWHM) of the absorption dip during MW irradiation is directly proportional to the temperature change of the sample (Türke 2010). To check this, the change of the quality factor (resonance position and FWHM of absorption dip) was monitored for irradiation times up to 120 s using additional directional couplers and a spectrum analyzer. The measured shifts were up to 3 MHz and no changes in FWHM (being ~ 40 MHz) were detected, meaning that long irradiation times did not affect the cavity quality factor.

Therefore, such measurements indicate that the cavity performance are stable during the irradiation time and the temperature of the sample does not change significantly, the latter being consistent with the observation $T_{1,n} \sim T_{\text{buildUp}}$.

S-1.5 Evaluation of DNP enhancements

DNP enhancements were evaluated by comparing the intensities recorded with (DNP) and without (Boltzmann) microwave irradiation. In order to take into account field inhomogeneities, which are not negligible in an EPR optimized magnet, signal integrals were considered. The enhancement is determined as:

$$\epsilon = \frac{I_{DNP}}{I_{Boltz}} \cdot \frac{n_{Boltz}}{n_{DNP}}$$

where I are the signal integral values, while n is the number of scans. In order to improve DNP data representation, the spectra are scaled to the same noise level by dividing by $(n)^{1/2}$. In this case, the enhancement is:

$$\epsilon = \frac{I_{DNP, scaled}}{I_{Boltz, scaled}} \cdot \sqrt{\frac{n_{Boltz}}{n_{DNP}}}$$

In order to overcome drifting of the static magnetic field at 1.2 T, Boltzmann signals were recorded within 1.5 h acquisition time. In some cases, multiple acquisitions were summed up to improve signal-to-noise ratio.

S-1.6 Summary of ^{13}C -DNP parameters

In the following sections, DNP parameters obtained at 1.2 T are listed for each compound. Leakage factor f , saturation factor s , ^{13}C enhancement ϵ are reported. The measurements were performed according to the procedures listed in the previous sections. Leakage factor f was calculated as $f = 1 - T_{1,n} / (T_{1,n})_0$, where $(T_{1,n})_0$ is the longitudinal relaxation time of the solvent without paramagnetic centres. The coupling factor ξ was calculated from s and f using the Overhauser equation (Equation (1) in the main text).

S-1.6.1 $^{13}\text{CCl}_4$ + TN

Table S1. 1.2 T DNP parameters of $^{13}\text{CCl}_4$ doped with TN. (1) Line width of EPR spectra at 34 GHz (spectra shown in Figure S6a). A line broadening is observed as a function of the concentration, which indicated a decreasing of $T_{2,e}$. (2) The saturation factor s displays a decrease towards high concentrations, correlating with the increasing line width. Experimental s values were compared with calculated ones in Figure S3. Errors on s and f are $< 5\%$, while for ϵ is $\sim 10\%$. Sample replicates were prepared to reproduce the results. Error on ξ is $\sim 15\%$.

C [mM]	T_{BuildUp} [s]	$T_{1,n}$ [s]	$T_{1,\text{dia}}$ [s]	$\Delta B^{(1)}$ [G]	$s^{(2)}$	f	ϵ	ξ
10	16.6	18.5	200	0.9	0.25	0.925	250 ± 30	- 0.41
20-30	5.1	6.7	200	1.7	0.175	0.965	160 ± 20	- 0.36
30	2.8	3.1	200	2.8	0.14	0.985	125 ± 15	- 0.34

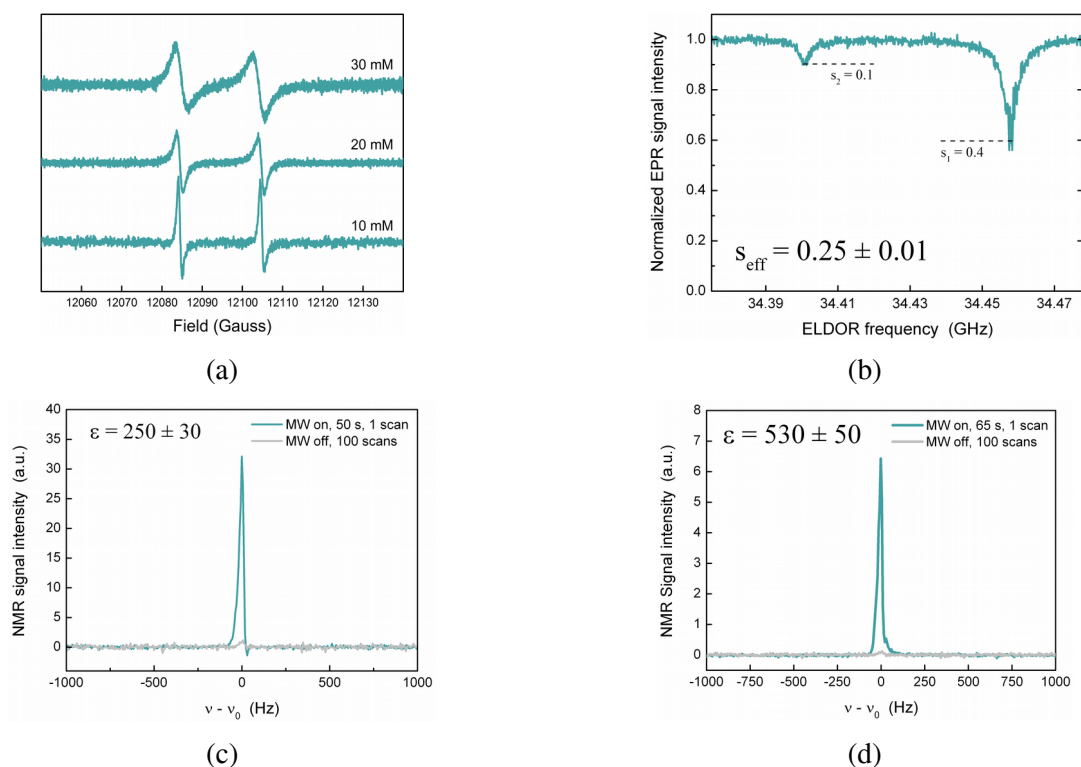


Figure S6. EPR spectra, saturation and enhancement of $^{13}\text{CCl}_4$ doped TN. (a) 34 GHz CW EPR spectra of TN in $^{13}\text{CCl}_4$ recorded for different radical concentrations (modulation amplitude 1 G, modulation frequency 100 kHz). For a radical concentration of 10 mM, the following measurements are presented: (b) ELDOR curve obtained by detecting on the low field line of TN ($\nu = 34.458$ GHz, ELDOR pulse length = 3 μs). The saturation values (s_1 , s_2 , and s_{eff}) are indicated. (c) ^{13}C -NMR signal enhancement recorded with 3 W MW amplifier. Enhanced spectrum was acquired by irradiating the low field EPR transition for 50 s. Recycle delay for thermal equilibrium signal was 60 s. (d) ^{13}C -NMR signal enhancement recorded with 40 W MW amplifier. MW irradiation was 65 s long. Recycle delay for thermal equilibrium signal was 60 s.

S-1.6.2 $^{13}\text{CCl}_4$ + FN2a

The fullerene-TEMPO FN2a was examined as alternative polariser. FN2a consists of a nitroxide functionalized with C_{60} and two additional side chains (Enkin 2015) (Figure S7a). Such molecule displays a longer $T_{1,e}$ resulting in more efficient saturation under comparable conditions, as previously demonstrated at 0.34 T (Enkin 2015).

The CW EPR spectrum at 34 GHz (Figure S7b) presents a line broadening of the higher field lines. The saturation factor was measured as described in Section S-1.2 (Figure S8). We found that within the experimental error the two experiments give the same saturation factor, as previously reported for lower field (Enkin 2015).

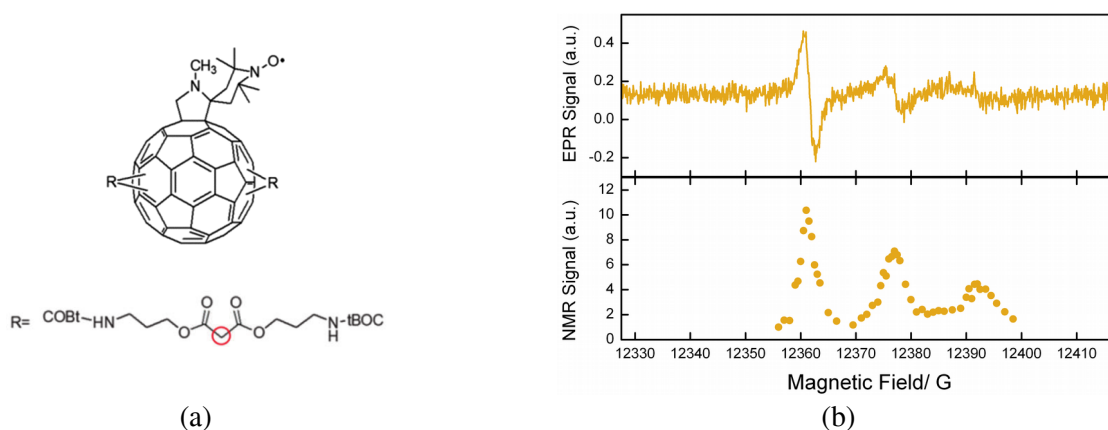


Figure S7. Structure of the FN2a molecule, EPR spectrum and enhancement profile in $^{13}\text{CCl}_4$. (a) Structure of nitroxide radical bound to C_{60} and with two side chains (FN2a). Side chains structure is shown and the circle indicates the link position. (b) (top) 34 GHz CW EPR spectrum of 1.5 mM FN2a in CCl_4 and (bottom) the correspondent enhancement field profile obtained with 10 s MW irradiation.

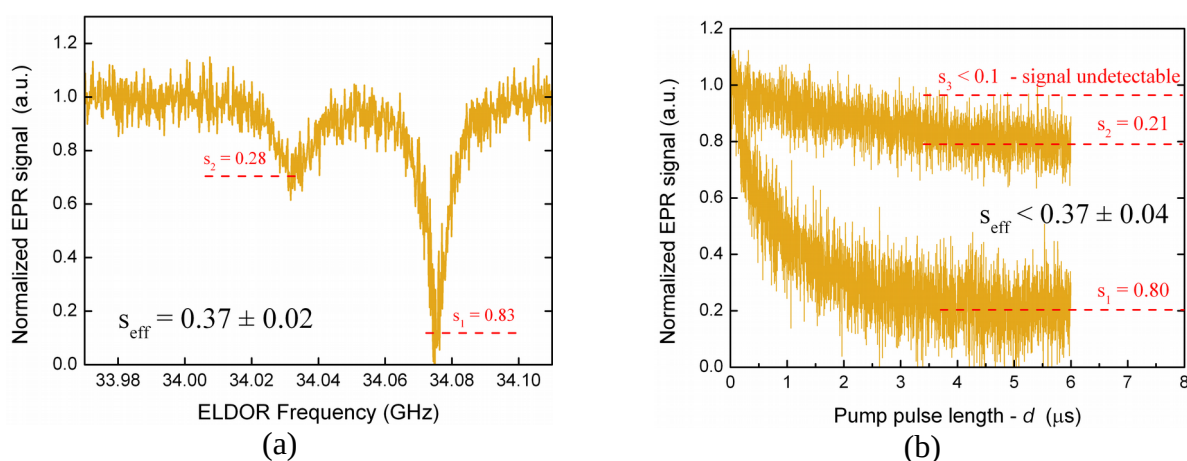


Figure S8. ELDOR and FID decay experiments for saturation measurements. Saturation factor was measured for FN2a in CCl_4 ($C = 1.5$ mM). (a) ELDOR was acquired as described in Figure S1, using an ELDOR pulse of 5 μs and detection on the low field line. (b) FID decay experiment is described in Figure S2. Due to very short T_2 , FID detection on the high field line was challenging. Therefore, s_3 can be estimated only as upper limit. The effective saturation factors s_{eff} obtained with the two methods are comparable within 10%.

Table S2. 1.2 T DNP parameters of $^{13}\text{CCl}_4$ doped with FN2a. Errors in s are 10% and in f are < 5%, while in ϵ is ~10%. Sample replicates were prepared to reproduce the results. Error on ξ is up to 25%.

C [mM]	T_{BuildUp} [s]	$T_{1,n}$ [s]	$T_{1,\text{dia}}$ [s]	f	s	ϵ	ξ
1.5	—	23.4	200	0.88	0.40	550 ± 50	- 0.60
5	12.2	13.6	200	0.93	0.37	510 ± 50	- 0.57
10	3.8	3.8	200	0.98	0.33	550 ± 80	- 0.65

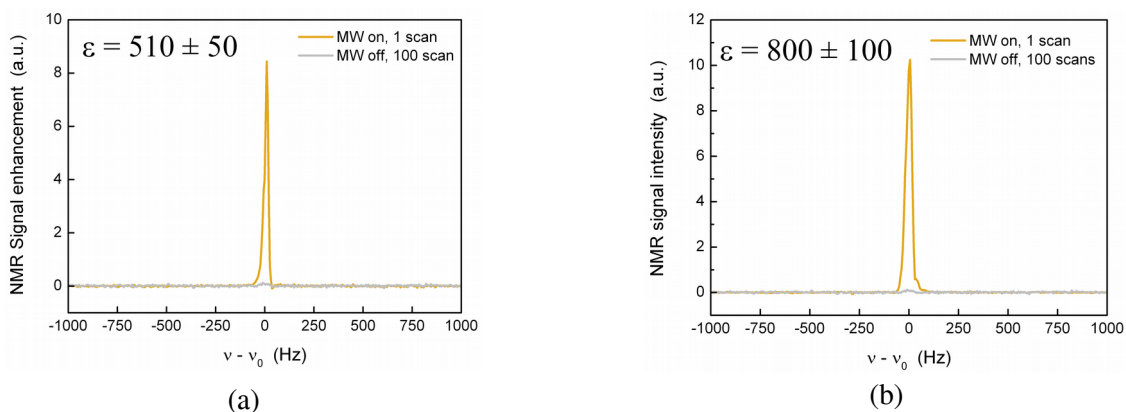


Figure S9. Enhancements of $^{13}\text{CCl}_4$ doped with 5 mM FN2a. (a) ^{13}C -NMR signal enhancement recorded with a 3 W MW amplifier and an irradiation pulse of 50 s. (b) ^{13}C -NMR signal enhancement recorded with a 40 W MW amplifier a MW irradiation pulse of 40 s. A 60 s recycle delay was used for thermal equilibrium NMR signals.

S-1.6.3 $^{13}\text{CHCl}_3$ + TN

Table S3. 1.2 T DNP parameters of $^{13}\text{CHCl}_3$ doped with TN. Errors on s and f are < 5%, while for ϵ is ~10%. Sample replicates were prepared to reproduce the results. Error on ξ is ~ 15%.

C [mM]	T_{buildUp} [s]	$T_{1,n}$ [s]	$T_{1,\text{dia}}$ [s]	f	s	ϵ	ξ
10	4.0	4.5	30	0.85	0.25	260 ± 40	- 0.46
10-20	2.9	3.9	30	0.85	0.18	200 ± 30	- 0.49

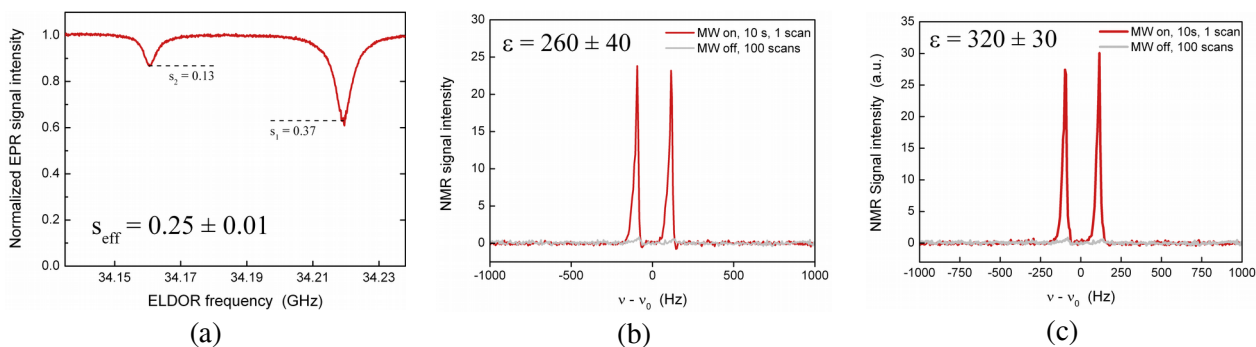


Figure S10. Saturation and enhancement of $^{13}\text{CHCl}_3$ doped with 10 mM TN. (a) ELDOR curve obtained detecting the low field line ($\nu = 34.219$ GHz, ELDOR pulse length = 3 μs) and saturation values. (b) ^{13}C -NMR signal enhancement. For DNP, the pump pulse was 10 s and for thermal equilibrium signal the recycle delay was 30 s. (c) Enhancement obtained with 40 W amplifier (irradiation time 10 s).

S-1.6.4 $^{13}\text{CHCl}_3$ + FN2a

Table S4. 1.2 T DNP parameters of $^{13}\text{CHCl}_3$ doped with FN2a. Errors in s are 10% and in f are < 5%, while in ϵ is ~10%. Sample replicates were prepared to reproduce the results. Error on ξ is up to 25%.

C [mM]	T_{BuildUp} [s]	$T_{1,n}$ [s]	$T_{1,\text{dia}}$ [s]	f	s	ϵ	ξ
4	3.1	3.5	30	0.89	0.30	370 ± 40	-0.53

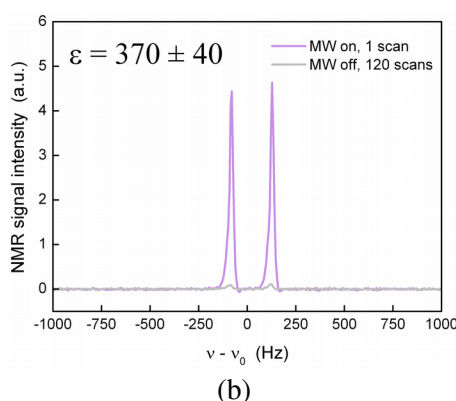


Figure S11. Saturation and enhancement of $^{13}\text{CHCl}_3$ doped with 4 mM FN2a. ^{13}C -NMR signal enhancement after 12 s of MW irradiation (3 W amplifier). Recycle delay for thermal equilibrium signal was 30 s.

S-1.6.5 Diethyl malonate-2- ^{13}C + TN

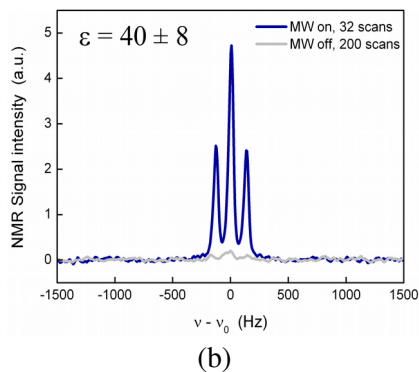
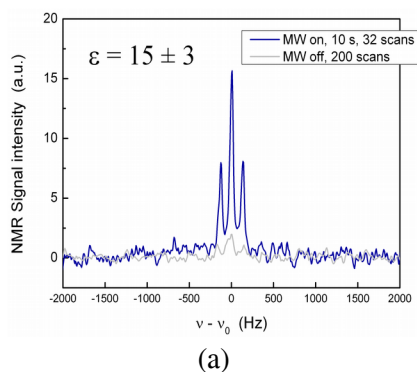


Figure S12. Diethyl malonate-2- ^{13}C doped with 10mM TN. Diethyl malonate was ^{13}C labeled in position 2 (CH_2 group). For the structure refer to Figure 2 of the main text. (a) ^{13}C -NMR signal enhancement recorded with 3 W amplifier. (b) Enhancement obtained with 40 W MW amplifier. In both cases, MW irradiation was 10 s long, with a recycle delay of 40 s. The recycle delay for thermal equilibrium signal was 30 s.

Table S5. 1.2 T DNP parameters of ^{13}C -2-diethyl malonate doped with FN2a. Errors on s and f are < 5%, while for ϵ is ~10%. Error on ξ is ~ 15%.

C [mM]	T_{BuildUp} [s]	$T_{1,n}$ [s]	$T_{1,\text{dia}}$ [s]	f	s	ϵ	ξ
~ 10	1.9	-	4.3	0.56	0.24	15 ± 3	-0.04

Table S6. Summary of ^{13}C -DNP parameters obtained from experiments at 1.2 T using TN as polarising agent (C = 10 mM). [a] Saturation factors at 1.2 T with 40 W MW power. Such values were calculated as: $s(40 \text{ W}) = s(3 \text{ W}) \cdot \epsilon(40 \text{ W}) / \epsilon(3 \text{ W})$, where $s(3 \text{ W})$ was measured via ELDOR experiments (Supplementary Information). Saturation factor in CHCl_3 is lower than CCl_4 due to reduction of the cavity Q-value. Errors in $s(1.2 \text{ T}, 3 \text{ W})$ and f are estimated < 5 %. Error in $s(1.2 \text{ T}, 40 \text{ W})$ is ~ 20%. [b] Errors in ξ at 1.2 T calculated from $s, f, \epsilon(3 \text{ W})$ are $\leq 15\%$.

1.2 Tesla	ϵ	$s^{[\text{a}]}$	f	ξ
$^{13}\text{CCl}_4$	530 ± 50	0.53	0.93	-0.41
$^{13}\text{CHCl}_3$	320 ± 30	0.30	0.85	-0.48
^{13}C -2-diethyl malonate	40 ± 8	0.59	0.56	-0.04

S-2 DNP at 9.4 T / 263 GHz / 100 MHz

S-2.1 Instrumentation and sample preparation

A liquid DNP home-built instrument, whose details have been previously reported (Denysenkov 2008, Denysenkov 2010, Neugebauer 2013), was used for DNP measurements at 9.4 T. NMR capabilities were provided by a Bruker Avance II console and a 9.4 T wide-bore NMR magnet. The MW source was a gyrotron (Gycom) operating at 263 GHz and having an output power of 10 W. The output of the gyrotron was then coupled with a cylindrical MW cavity. Frequency tuning capability of the gyrotron (65 MHz) was crucial for optimizing each DNP experiment.

Performance of the spectrometer for DNP at high fields depends strongly on the efficiency of the probe head which is mainly defined by the resonance structure. Our approach is a double resonance structure similar to one described by Weis et al. (Weis 1999) and re-scaled later to 263 GHz for protons (Denysenkov 2008). The resonance structure consist of a cylindrical cavity made of copper tape forming a helical six-turn coil of 1.5 mm inner diameter, which serves also as rf coil (Figure S13). The leads of the coil are connected to an rf matching circuit tuned to the ^{13}C NMR frequency, i.e. 100 MHz. This arrangement permits rf penetration and is a concept previously explored by Gruber et al. (Gruber 1974) at low frequencies. The microwave cavity is equipped with two plungers made of MACOR ceramics with flat caps coated with a silver thin film. One plunger is movable for MW frequency tuning. Microwave coupling is achieved through an elliptical iris via a WR-4 waveguide that is attached to the helix in the middle, grounding the coil at this position with respect to rf (Denysenkov 2008). In the case of ^{13}C -DNP, the cylindrical TE_{013} mode of the cavity was chosen instead of TE_{011} mode to increase space between plungers up to 4.8 mm, allowing for a larger amount of sample and a higher NMR signal. The angular electric field distribution of TE_{01n} modes is maintained since the gaps between turns are almost parallel to the surface currents. Moreover, the gaps serve as a filter of spurious modes, so that the cavity shows a clear microwave spectrum of only TE_{01n} modes. The resonance structure was simulated for microwave frequency response, magnetic field distribution, and calculations of a Q-factor as well as a B_1 value by using CST MW Studio Suite (Darmstadt, Germany).

Samples were inserted in capillaries having 160 μm outer diameter and 100 μm inner diameter. The irradiated sample volume is ~ 35 nL. Due to the tiny capillary size, a degassing procedure with freeze-pump-thaw cycle was not feasible. A previous extensive study (Neugebauer 2013) indicates that a polarising agent concentration of 100 mM leads to high saturation factors ($s \geq 0.8$). All DNP measurements were performed under CW MW irradiation condition.

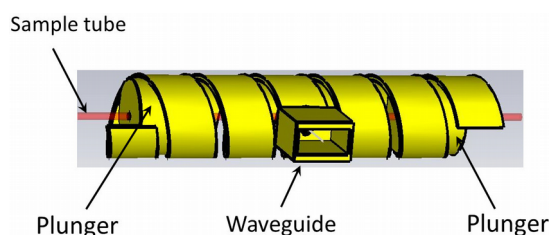


Figure S13. Schematic drawing of the MW and rf double resonance structure. For size and details please refer to Denysenkov et al., 2008 (Denysenkov 2008).

S-2.2 MW saturation and temperature effect

Previous DNP studies in water as well as organic solvents showed that the saturation factor is accessible by measuring the residual paramagnetic shift under DNP conditions with respect to an undoped sample (Neugebauer 2013, Neugebauer 2014). ^{13}C -NMR spectra of $^{13}\text{CCl}_4$ doped with 100 mM TN were compared with a thermal equilibrium signal recorded for undoped $^{13}\text{CCl}_4$ (Figure S14). At thermal equilibrium the two signals show a chemical shift (~ -1.3 ppm) rising from the paramagnetic shift. This difference is compensated under MW irradiation, where the population difference on the electronic levels is almost saturated. According to previous studies, this suggests that in our configuration and under DNP condition we are close to the equipopulation of the electronic spin levels, which leads to a saturation close to 1 for CCl_4 . However, for samples with higher dielectric losses the saturation factor will be slightly decreased.

A chemical shift with respect to the reference signal (i.e. MW off and no polarising agent) can be observed ($\sim +0.15$ ppm) (Figure S14a). Such shift could be ascribed to a temperature effect. According to a measurements of a shift of ~ 0.15 ppm every 40°C (Figure S14b), we conclude that under DNP condition the sample could increase the temperature up to 70°C .

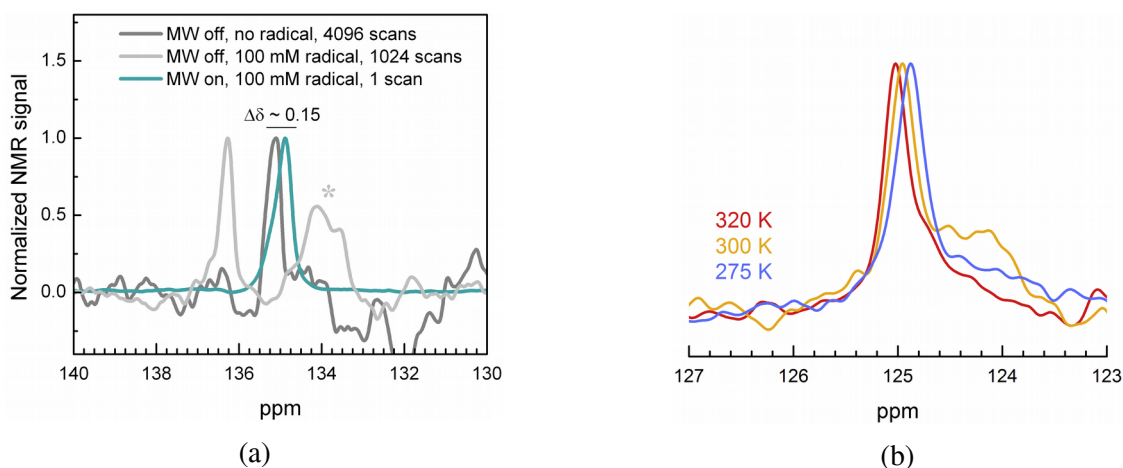


Figure S14. Paramagnetic and temperature shifts. (a) NMR spectra of $^{13}\text{CCl}_4$ with and without polarising agent recorded with DNP setup under different conditions. (b) ^{13}C -NMR spectra of CCl_4 recorded at different temperatures with a commercial 400 MHz liquid state probe head (Bruker BBI). Please note that in the last case the temperature shift is negative due to a different probe geometry, where the sample is placed vertically instead of horizontally, as in the DNP case.

S-2.3 ^{13}C -NMR enhancements

NMR signal enhancements were quantified by comparing signal integrals of spectra acquired with and without microwave, as previously described (Section S-1.5). Due to resonator construction, part of the sample is located outside the resonator, but still within the NMR coil detection range. For this reason, Boltzmann spectra display a second signal about 2 to 4 ppm apart from the reference and that is not enhanced with DNP (Neugebauer 2014). Such peaks are labeled with an asterisk and not considered in data analysis. The error calculated on the enhancement value is related to the signal-to-noise ratio of the spectra and does not include the temperature effect.

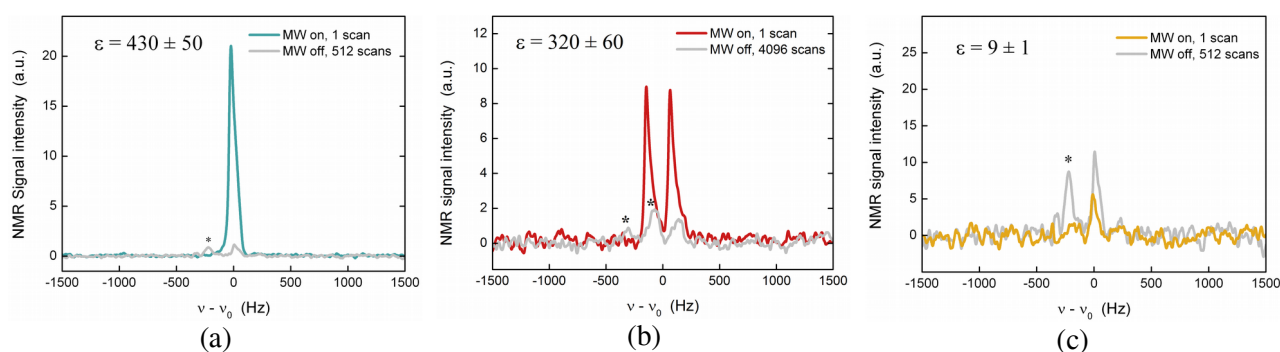


Figure S15. ^{13}C -DNP on CCl_4 and CHCl_3 at 9.4 Tesla. Signal enhancements of (a) $^{13}\text{CCl}_4$ and (b) $^{13}\text{CHCl}_3$ and doped with 100 mM TN. (c) DNP on $^{13}\text{CCl}_4$ doped with FN2a.

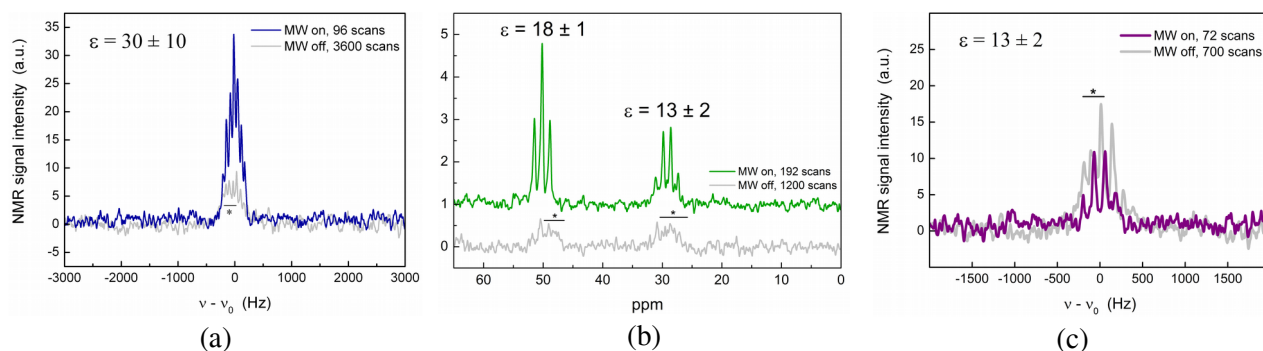


Figure S16. ^{13}C -DNP on organic molecules at 9.4 T. (a) ^{13}C -DNP spectrum for ^{13}C -2 of the system ^{13}C -1-2-3-Diethyl malonate. No enhanced signal was detected for ^{13}C -1 and ^{13}C -3. The recycle delay used was 15 s both for DNP and thermal equilibrium. (b) DNP enhancements in ^{13}C -2-4-ethyl acetoacetate (recycle delay 10 s). The peak at ~29 ppm corresponds to ^{13}C -4, while the one at ~50 ppm corresponds to ^{13}C -2. (c) Pyruvic acid dissolved in di-isopropyl ether (77:100 M/M). Pyridine is added (1.5:1 M/M) to protect the nitroxide radical decay. No evidence of radical quench was recorded during the measurement time, being the enhancement stable over time. In order to limit the heating effect, for each measurement 16 scans were averaged (~4 min) under continuous wave MW irradiation. The waiting time between each slot was 5-10 min without MW irradiation.

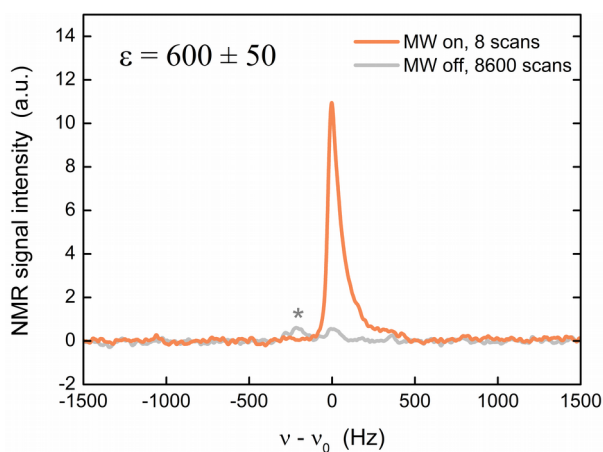


Figure S17. ^{13}C -DNP on CBr_4 at 9.4 Tesla. $^{13}\text{CBr}_4$ was dissolved in CCl_4 until saturation (~ 30 mg in $30\ \mu\text{L}$) and doped with 100 mM TN. Acquisitions were performed with 5 s recycle delay.

S-2.4 ^{13}C -NMR line width under DNP conditions

NMR line widths were measured for different polarising agent concentrations in diethyl malonate. One experiment was performed on a high-resolution liquid state NMR probe (Figure S18a). It revealed a slight increase in line width with concentration of the polarising agent ($\Delta_{\text{max}} \sim +4$ Hz). The line width achieved on the DNP setup at 9.4 Tesla has a typical FWHM of ~ 30 Hz (Figure S18b). FWHM was found approximately constant from 10 to 100 mM under DNP conditions, revealing that the contribution of the concentration of the polarising agent to the FWHM does not affect NMR resolution significantly.

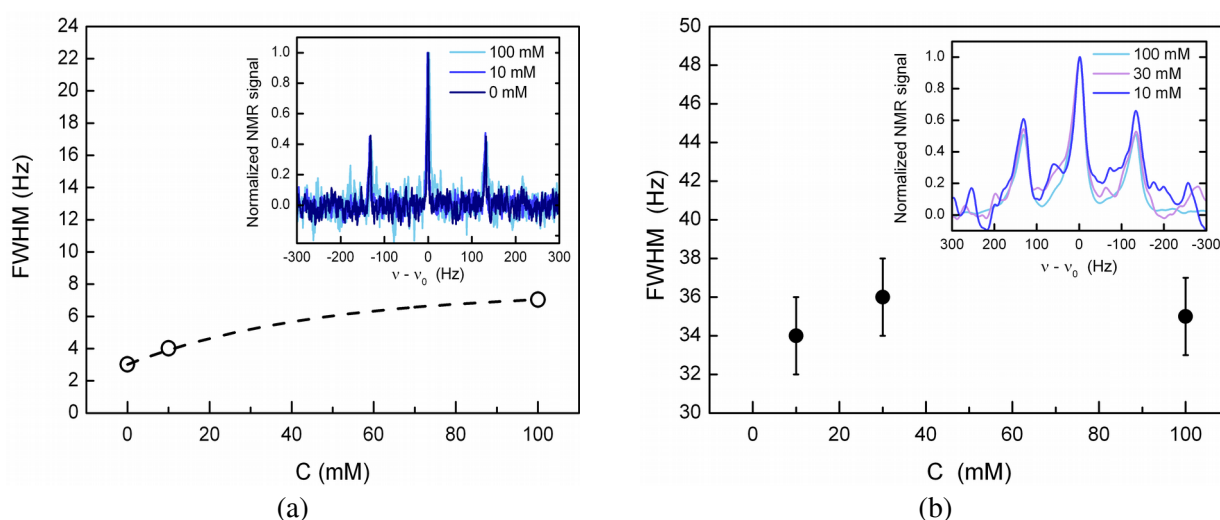


Figure S18. NMR line width in diethyl malonate (position 2) at 9.4 Tesla. FWHM measured in diethyl malonate is reported as a function of polarising agent concentration (a) measured in a high resolution liquid state NMR system and (b) under MW irradiation in a DNP setup. The central line was taken as reference. The insets show a magnification of the spectra.

S-2.5 EPR spectra at 263 GHz

CW EPR spectra at 9.4 Tesla (Figure S19) were recorded on a Bruker E780 spectrometer equipped with a 100 mW amplifier multiplier chain (Virginia Diodes) and a non-resonant probe head. Radical concentration chosen was ~ 100 mM, as for DNP measurements.

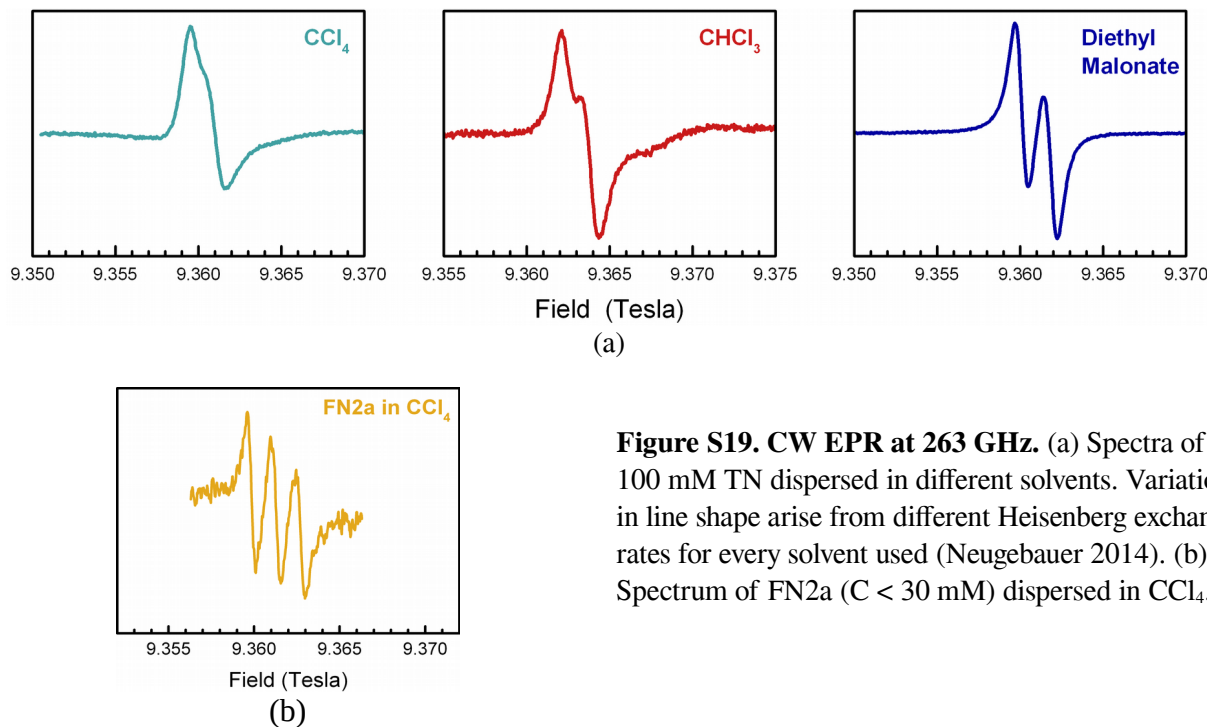


Figure S19. CW EPR at 263 GHz. (a) Spectra of 100 mM TN dispersed in different solvents. Variations in line shape arise from different Heisenberg exchange rates for every solvent used (Neugebauer 2014). (b) Spectrum of FN2a ($C < 30$ mM) dispersed in CCl_4 .

S-2.6 Spin count and NMR sensitivity

The detection limit of the instrument at 9.4 T was quantified by calculating the number of detected spins (Table S7). These results were compared with the performance of a standard instrument for high-resolution NMR operating at 9.4 T/ ^1H -400 MHz (Bruker Avance III). The signal-to-noise ratio (SNR) was also compared. Despite the number of detected spins on the DNP instrument is more than one order of magnitude smaller than the one in a standard spectrometer, the SNR results larger by at least a factor of 10. Although the analytes concentration remains an issue for our DNP instrument, we can observe that Overhauser DNP has the potential to enable the NMR detection of low concentrated substances.

Table S7. Spin quantitation at 9.4 T on different instruments. [a] DNP enhanced signal. [b] Measurement performed with a 30° pulse.

Compound	9.4 T DNP		High-resolution ¹ H-400 MHz spectrometer	
	<i>Sample volume = 35 nL</i>		<i>Sample volume = 200 μL</i>	
	¹³ C fully labeled		¹³ C natural abundance	
	Detected spins	SNR in 1 scan ^[a]	Detected spins	SNR in 1 scan ^[b]
CCl ₄	2 × 10 ¹⁷	100	1 × 10 ¹⁹	0.7
Diethyl malonate	1 × 10 ¹⁷	1.6	8 × 10 ¹⁸	0.5

Table S8. ¹³C-DNP parameters obtained from experiments at 9.4 T using TN as polarising agent (C = 100 mM). Coupling factors ξ were calculated with $s = 1$ for CCl₄, and $s = 0.8$ for CHCl₃ and diethyl malonate estimated as lower limit of s_{CCl_4} . Error in s was ~ 10%. From relaxation data at 9.4 T recorded on a liquid state 400 MHz NMR spectrometer the leakage factor results $f_{\text{CCl}_4} = 0.98$ ($T_{1,n} = 1.5$ s, $(T_{1,n})_0 = 73$ s), $f_{\text{CHCl}_3} = 0.93$ ($T_{1,n} = 1.0$ s, $(T_{1,n})_0 = 13$ s), and $f_{\text{malonate}} = 0.68$ ($T_{1,n} = 1.0$ s, $(T_{1,n})_0 = 3.2$ s), with an error < 5%. Due to the temperature effect, the coupling factor ξ can be considered as lower limit and an asymmetrical error bar (+40%,-30%) can take into account such effect (see Section S-4.1 for details).

9.4 Tesla	ε	s	f	ξ
¹³ CCl ₄	430 ± 50	1.0	0.98	-0.17
¹³ CHCl ₃	320 ± 60	0.8	0.93	-0.16
¹³ C-2-diethyl malonate	30 ± 10	0.8	0.68	-0.017

S-3 DNP at 14 T / 395 GHz / 150 MHz

DNP experiments were performed at 14 T on Bruker Avance III ^1H -600 MHz spectrometer equipped with a 395 GHz gyrotron as MW source. Samples were degassed with freeze-pump-thaw cycles and then transferred under argon atmosphere in a 3.2 mm sapphire rotor. Rotors were then sealed with a teflon spacer and the drive tip. In this way, samples could stay oxygen free for days, as verified by reproducible enhancements over time. In order to limit temperature gradients inside the sample under MW irradiation, the rotor was only partially filled with 10-25 μL , corresponding to 30% – 70% of the total volume ($\sim 36 \mu\text{L}$). Under these conditions, sample spinning from 3 to 5 kHz was achievable. ^{13}C abundance in the tested samples was 1%-5%.

The DNP setup at 14 T is not equipped with a MW cavity. As a consequence, MW B_1 is not enhanced at the sample position, resulting in a poor saturation factor s (Equation S1 and S2) and also a non-negligible heating effect caused by the electric fields. The latter can be controlled by enabling cold N_2 gas ($T = 200 \text{ K}$, flow rate = 1870 L/h) flowing on the sample. The temperature at the sample position was calibrated measuring the temperature shift of a standard reference sample, i.e. KBr_4 , inserted at the bottom of a rotor filled with CCl_4 . The measured values were in agreement with the ones displayed by the temperature control unit, the difference being $< 3 \text{ K}$. DNP experiments were performed under CW MW irradiation with a recycle delay of 15 s.

DNP results on CCl_4 and CHCl_3 are shown in Figure S21.

Fullerene nitroxide FN2a in CCl_4 (10 mM) was tested as well, giving a ^{13}C -NMR enhancement $\varepsilon \sim 3$, as shown in Figure S22a. The role of the halogen as polarization transfer mediator was investigated by choosing $^{13}\text{CBr}_4$ as target compound. A solution of 6.4 mg CBr_4 (5% ^{13}C labeled) and 100 μL of CCl_4 was doped with 10 mM TN. The enhancement was $\varepsilon = 35 \pm 3$ (Figure S22b). Due to inhomogeneous irradiation and a strong temperature dependence of the chemical shift, a line broadening is observed under DNP conditions as a consequence of temperature gradient inside the rotor.

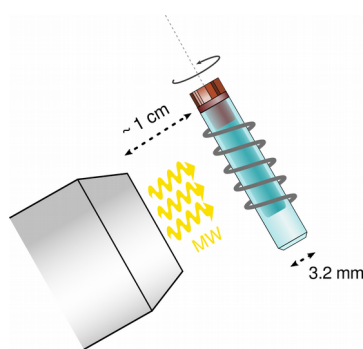


Figure S20. Schematic drawing of the DNP-MAS probe. For details please refer to Rosay, et al. (Rosay 2016).

Table S9. DNP parameters at 14 T.

Polarising agent	Solvent	ϵ	ξ (predicted)
TN	CCl_4	23 ± 5	- 0.1
TN	CHCl_3	17 ± 2	- 0.07

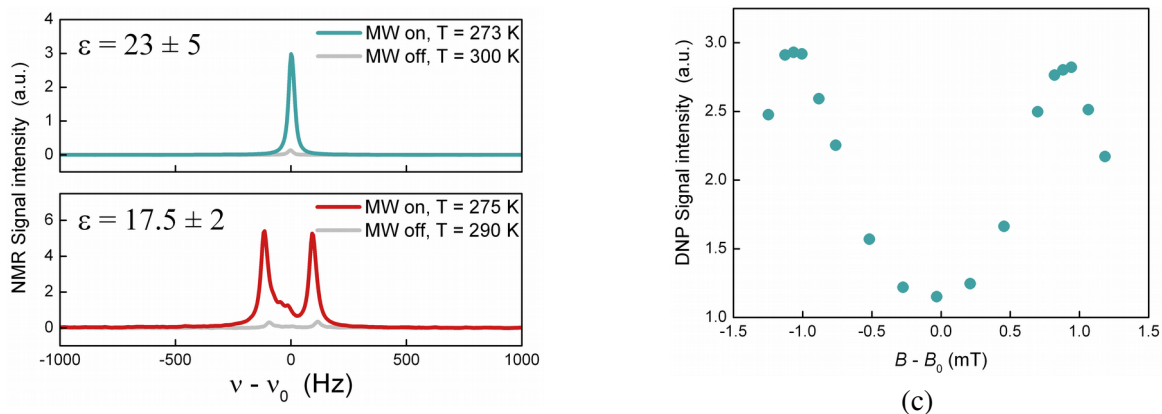


Figure S21. ^{13}C -DNP on CCl_4 and CHCl_3 at 14 Tesla. Enhancement obtained at 14 T on (a) CCl_4 and (b) CHCl_3 , both doped with 10 mM $^{\text{TN}}$. (c) Enhancement field profile (in arbitrary units) obtained sweeping the room temperature z-shim, that has a maximum sweep range of ~ 2.5 mT, enough for covering $^{\text{TN}}$ EPR spectrum (hyperfine coupling $A \sim 60$ MHz ~ 1.8 mT). In the profile, two peaks, corresponding to the two EPR lines, are clearly distinguishable.

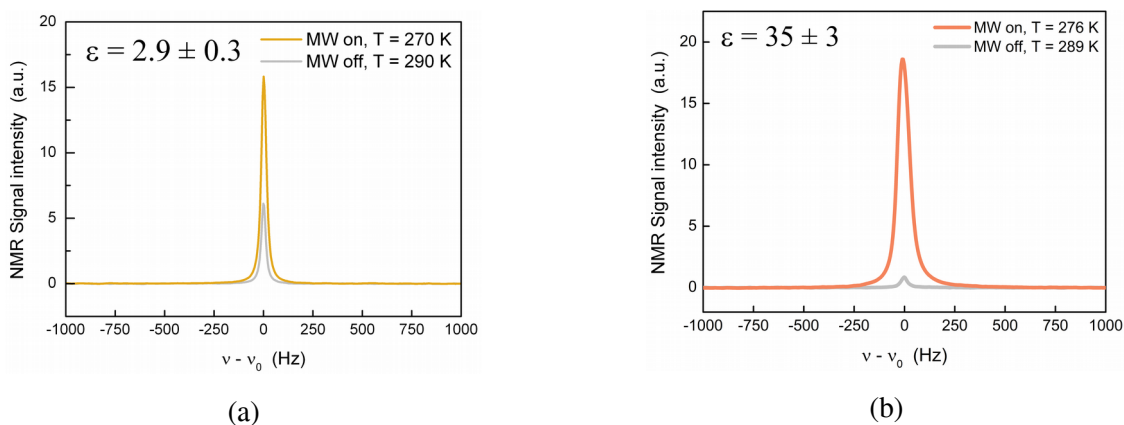


Figure S22. (a) ^{13}C -NMR enhancement at 14 T of CCl_4 doped with FN2a. (b) ^{13}C -DNP of CBr_4 doped with $^{\text{TN}}$. Under MW irradiation, a line broadening due to temperature gradients is observed.

S-4 Mechanistic model for the coupling factor

The coupling factor ξ (Equation 2 main text) can then be rewritten as (Bennati 2010, Ravera 2016):

$$\xi = \frac{5}{7} \left[1 - \frac{3k' J_{diff}(\omega_n, \tau_d)}{R_{1,cont} + R_{1,diff}} \right] - \frac{12}{7} \frac{R_{1,cont}}{R_{1,cont} + R_{1,diff}} \quad (S3)$$

where $R_{1,cont}$ and $R_{1,diff}$ are the contributions to the nuclear relaxation rate arising from contact and translational diffusion, respectively.

The dipolar contribution originates from through space magnetic interaction between electron and nuclear spins and is consequently modulated by diffusion. The *force-free* diffusion model proposed by Freed (Freed 1978) assumes that the interacting spins are at the center of spherical molecules that diffuse with respect to each other. The spectral density describing the process is (Polnaszek 1984):

$$J_{diff}(\omega, \tau_d) = \frac{1 + 5z/8 + z^2/8}{1 + z + z^2/2 + z^3/6 + 4z^4/81 + z^5/81 + z^6/648} \quad \text{with } z = \sqrt{2\omega\tau_d} \quad (S4)$$

The correlation time for translational diffusion is defined as $\tau_d = r_d^2/D$, where r_d is the distance between the centers of the two spherical spin-bearing molecules (distance of closest approach) and D is the diffusion coefficient.

The corresponding relaxation rate is defined as:

$$R_{1,diff} = k [7 J_{diff}(\omega_e, \tau_d) + 3 J_{diff}(\omega_n, \tau_d)] \quad (S5)$$

with

$$k = \frac{32000\pi}{405} \left(\frac{\mu_0}{4\pi} \right)^2 \frac{N_A C \gamma_n^2 g_e^2 \mu_B^2 S(S+1)}{r_d D} \quad (S6)$$

where N_A is the Avogadro number, C is the polarising agent concentration and γ_n is the gyromagnetic ratio in rad·Hz/T. Scalar coupling relies on Fermi contact interaction, which happens through randomly distributed collisions between polarizing agent and target molecules. The intermolecular hyperfine coupling A is then time dependent, being $A \neq 0$ whenever a collision occurs. Two time-constants characterize this process: *i*) the collision duration $2 \cdot \tau_i$, and *ii*) the mean time between collisions τ_p . A simple description of this process is given by the pulse model introduced by Noack and Müller-Warmuth (Müller-Warmuth 1968):

$$J_{cont}(\omega_e, \tau_i) = \frac{\langle A^2 \rangle}{\hbar^2 \tau_p} [\tau_i \exp(-\omega_e \tau_i)]^2 \quad (S7)$$

where $\langle A^2 \rangle$ is the mean square amplitude of the contact coupling constant, ω_e is the electron Larmor frequency in rad/s and τ_i is the duration of molecular contact of type i . This leads to the relaxation rate (Abragam 1962):

$$R_{1,cont} = \frac{2}{3} S(S+1) J_{cont}(\omega_e, \tau_i) \quad (S8)$$

The equation S3 was used to describe the coupling factors as a function of the field.

CCl₄. In the case of CCl₄, the polarization transfer between the free electron of the polarising agent and ¹³C is mediated only by chlorine atom. The coupling factor for CCl₄ can be expressed as:

$$\xi_{\text{CCl}_4} = \frac{5}{7} \left[1 - \frac{3 k^{\text{CCl}_4} J_{\text{diff}}^{\text{CCl}_4} (\omega_n, \tau_d^{\text{CCl}_4})}{R_{1,\text{cont}}^{\text{CCl}_4} + R_{1,\text{diff}}^{\text{CCl}_4}} \right] - \frac{12}{7} \frac{R_{1,\text{cont}}^{\text{CCl}_4}}{R_{1,\text{cont}}^{\text{CCl}_4} + R_{1,\text{diff}}^{\text{CCl}_4}} \quad (\text{S9})$$

The free parameters in the simulation are: *i*) the contact time $2 \cdot \tau_{i,\text{CCl}_4}$; *ii*) the prefactor of Equation S7, $F_{\text{CCl}_4} = \langle A^2 \rangle / (\hbar^2 \tau_{p,\text{CCl}_4})$; *iii*) the distance of minimum approach $r_{d,\text{Cl}}$; *iv*) the concentration *C* of the polarising agent (in our case 0.02 M). In order to simulated the experimental data, a single type of contact was sufficient. The scalar contribution results in the sub-picosecond range ($\tau_{l,\text{CCl}_4} = 0.5$ ps). Such short time scale is typical of elastic encounters between the polarizing agent and the target molecule. The distance of closest approach for the diffusion is $r_{d,\text{Cl}} = 4.0$ Å, being slightly lower than the one obtained by DFT calculation (Table S11).

Although it is not possible to separate contact and diffusion contributions analytically in Equation S3, it is recognizable that the first term of the sum is primarily determined by translational diffusion, while the second one accounts mainly for the contact interaction. The field dependence of these two terms is shown in Figure S23.

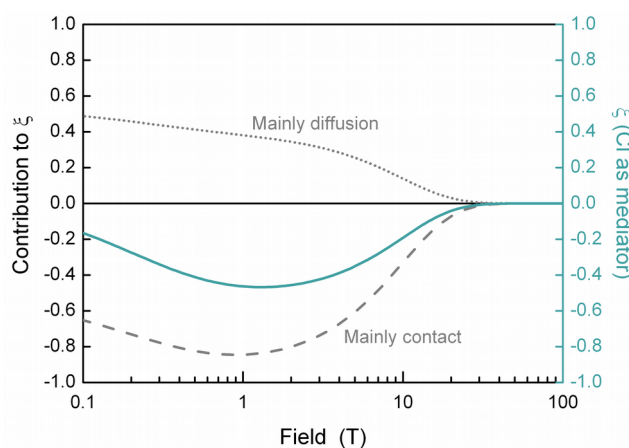


Figure S23. Diffusion and contact contributions to the coupling factor for CCl₄/¹³C. Coupling factor as a function of the magnetic field for CCl₄ doped with ¹³C was calculated with Equation S3 (solid line). The first term of Equation S3 (dot line) is mainly governed by diffusion contribution, and the second one (dash line) primarily describes the contact.

CHCl₃. In the case of CHCl₃ the polarization transfer is mediated either by Cl or H. To take into account both contributions, the coupling factor for CHCl₃ was calculated considering ³/₄ of the CCl₄ contributions, for which the Cl atom is the only mediator. The previous parameters τ_{l,CCl_4} , F_{l,CCl_4} and $r_{d,\text{Cl}}$ were adopted, while the diffusion coefficient *D* was scaled to the chloroform one.

An additional term arises from hydrogen. The contribution mediated by the H uses a second set of parameters: $r_{d,\text{H}}$, the distance of closest approach at the H of CHCl₃ for translational diffusion, which is shorter than $r_{d,\text{Cl}}$; $\tau_{2,\text{H}}$, the contact time between the radical (O atom) and the H atom; $F_{2,\text{H}}$, the prefactor of the contact density function accounting for the collisions mediated by H. Consequently, Equation S9 is modified as follows:

$$\xi_{\text{CHCl}_3} = \frac{5}{7} \left[1 - \frac{0.75 \cdot 3 k^{\text{CCl}_4} J_{\text{diff}}^{\text{CCl}_4}(\omega_n, \tau_d^{\text{CCl}_4}) + 3 k^{\text{H}} J_{\text{diff}}^{\text{H}}(\omega_n, \tau_d^{\text{H}})}{0.75 \cdot R_1^{\text{CCl}_4} + R_{1,\text{cont}}^{\text{H}} + R_{1,\text{diff}}^{\text{H}}} \right] - \frac{12}{7} \frac{0.75 \cdot R_{1,\text{cont}}^{\text{CCl}_4} + R_{1,\text{cont}}^{\text{H}}}{0.75 \cdot R_1^{\text{CCl}_4} + R_{1,\text{cont}}^{\text{H}} + R_{1,\text{diff}}^{\text{H}}} \quad (\text{S10})$$

where $R_1^{\text{CCl}_4} = R_{1,\text{cont}}^{\text{CCl}_4} + R_{1,\text{diff}}^{\text{CCl}_4}$. The values of the parameters accounting for the hydrogen contribution are reported in Table 2 in the main text. In order to visualize the contributions from Cl and H individually, the Equation S3 was used with the two sets of parameters, i.e. τ_{1,CCl_4} , F_{1,CCl_4} , $r_{d,\text{Cl}}$ and $\tau_{2,\text{H}}$, $F_{2,\text{H}}$ and $r_{d,\text{H}}$. The resulting curves are shown in Figure 3 in the main text.

Diethyl malonate. The field dependence of the coupling factor of diethyl malonate was interpreted in the framework of the pulse model. The ξ values are in this case lower (in absolute value) than the ones reported for CCl_4 and CHCl_3 . Given the different chemical environment, consisting of two protons forming a CH_2 group, we expect a larger dipolar contribution as a consequence of the short distance of closest approach. Furthermore, although the sign of ξ remains negative over the whole field range, the experimental points suggest a non-monotonous behavior. Therefore, this suggests that the scalar interaction is dominant and has two major contributions characterized by different correlation times, as for CHCl_3 . The first one results to be modulated on a fast time scale and has to be ascribed to elastic intermolecular collisions. This is responsible of the scalar enhancement observed at high fields (3 - 9.4 T). The second one arises from the presence of the hydrogen atoms, which favors the formation of a hydrogen bond-like complexes whose contact time is characterized by tens of ps.

Table S10. Parameters used for simulating the coupling factor field dependence.

	$(F_1)^{1/2} (\text{s}^{-3/2})^{[a]}$	$\tau_1 (\text{ps})$	$(F_{2,\text{H}})^{1/2} (\text{s}^{-3/2})^{[a]}$	$\tau_{2,\text{H}} (\text{ps})$	$r_d (\text{\AA})$	$\tau_d (\text{ps})^{[c]}$
CCl_4	1.3×10^{12}	0.5	-	-	4.0	114
CHCl_3	1.3×10^{12}	0.5	5×10^{11}	12	4.0 / 3.4 ^[b]	53 / 39 ^[c]
Diethyl malonate	7.5×10^{11}	0.5	9.5×10^{10}	20	2.8	92

[a] Prefactor of the contact density function J_{cont} , i.e. $F = \langle A^2 \rangle / (\hbar^2 \tau_p)$. [b] The distance of closest approach in the case of chloroform depends on the mediator, Cl or H. [c] The correlation time for translational diffusion was calculated as $\tau_d = r_d^2 / D$, where D is the diffusion coefficient. For the three compounds one has: $1.4 \times 10^{-9} \text{ m}^2/\text{s}$ for CCl_4 (Hexem 1976), $3.0 \times 10^{-9} \text{ m}^2/\text{s}$ for CHCl_3 (Kovacs 1990), and $8.5 \times 10^{-10} \text{ m}^2/\text{s}$ (Buffle 2007) for diethyl malonate. The resulting τ_d reflects the local diffusion, strictly dependent on the chemical environment (Polnaszek 1984).

Table S11. Distance of closest approach for investigated compounds.

mediator	$^{13}\text{C} - \text{mediator}^{[a]}$	mediator - O ^[b]	total ^[c]	$r_d^{[c]}$
Cl	1.7 \AA	3.0 \AA	4.7 \AA	4.0 \AA
H	1.0 \AA	2.0 \AA	3.0 \AA	3.4 \AA

[a] bond length; T.L. Cottrell, *The Strengths of Chemical Bonds*, 2nd ed., Butterworths, London, 1958; S.W. Benson, *J. Chem. Educ.*, 42, 502 (1965). [b] distance from DFT calculations by Liu *et al.* (Liu 2017) [c] total distance ^{13}C -mediator. [d] r_d used for simulating the experimental coupling factor ξ .

S-4.1 Influence of temperature on the coupling factor at high fields

The temperature was controlled at 1.2 T, 3.4 T (checked with nuclear relaxation times), and 14 T (stabilized with nitrogen flow and controlled with KBr as temperature probe). At 9.4 T the sample temperature raises up to 70°C. This results in a higher diffusion coefficient D , as reported in literature (Hexem 1976), and D almost doubles when temperature increases of $\sim <50$ K. As previously reported (Bennati 2010, Neugebauer 2013), the dipolar relaxation rate $R_{1,diff}$ drops as temperature increases, as a consequence of the dependency of $R_{1,diff}$ on D (Equation S5). Due to the competing effect between scalar and dipolar relaxation (Equation S9), the overall value of the coupling factor ξ decreases when D increases in $R_{1,diff}$. Despite an influence of such parameter on the scalar contribution is not excluded (although it is not clear yet) (Parigi 2018), we simulated the coupling factor values of CCl_4 / TN in the high field region lower values of D (Figure S24), in order to quantify the overestimation of ξ at 9.4 T. The result show that the temperature contribution could be large, but within the error bar assumed for the data point at 9.4 T (Table . Moreover, the coupling factor curve does not display any particular feature at high field, where ξ smoothly goes to zero, meaning that the analysis and the conclusions reported in the manuscript are not significantly affected by temperature.

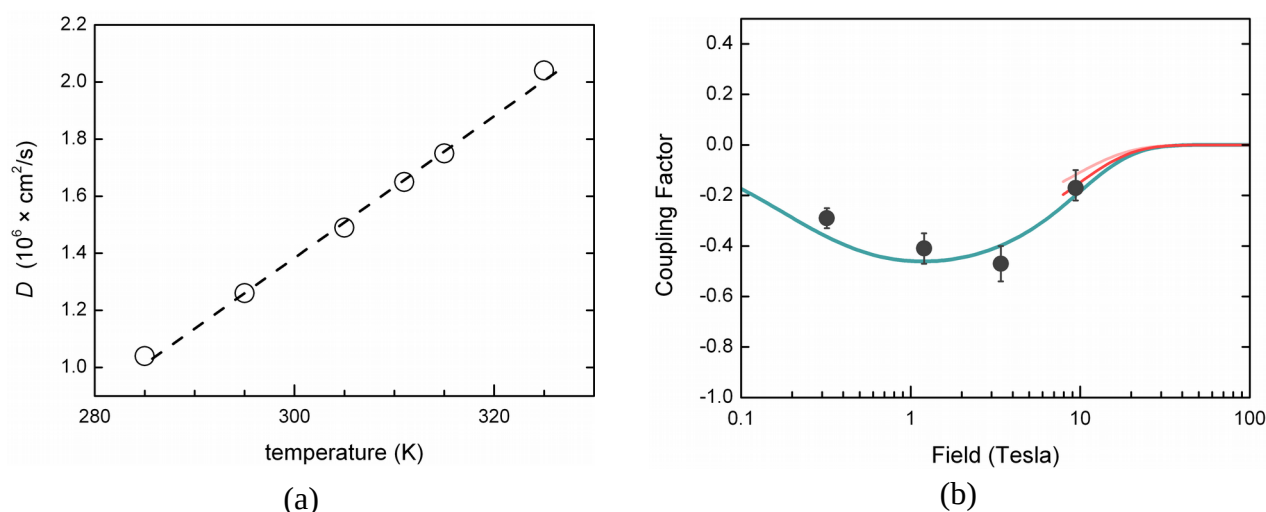


Figure S24. Temperature dependency of D and ξ . (a) Diffusion coefficient of CCl_4 as a function of the temperature (Hexem 1976). (b) High field coupling factors calculated for $D = 0.75 \cdot D_{\text{CCl}_4}$ (red) and $D = 0.5 \cdot D_{\text{CCl}_4}$ (pink).

S-5 DFT calculations of ^{13}C hyperfine coupling

The DFT package Gaussian 09⁸ was used for both geometry optimization and single point energy calculation. The geometry optimizations were performed at the B3LYP level of theory using 6-311++G** basis set. The single point energy calculation was performed at B3LYP or BLYP level using 6-311++G(3df,3pd) basis set. For CCl_4/TN and CBr_4/TN a polarization continuum model (PCM) implemented in Gaussian was used to account for the dielectric properties of the solvents.

Table S12. Distances and ^{13}C hyperfine coupling constants from DFT for halogenated compounds.

CCl_4		CBr_4	
$d_{\text{O-Cl}}$ (Å)	Fermi contact hyperfine constant on ^{13}C (MHz)	$d_{\text{O-Br}}$ (Å)	Fermi contact hyperfine constant on ^{13}C (MHz)
2.96	4.65	2.94	10.04

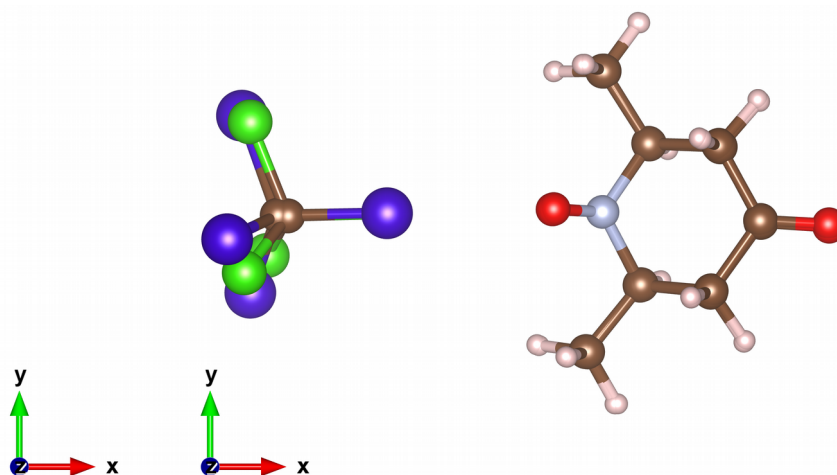


Figure S25. Geometry-optimized orientations for CCl_4/TN and CBr_4/TN .

Table S13. Coordinates of DFT optimized geometries for halogenated compounds.

TN / CCl_4				TN / CBr_4			
N	2.184000	0.070000	-0.255000	N	3.397000	0.058000	-0.274000
C	2.845000	-1.219000	-0.547000	C	4.077000	-1.225000	-0.555000
C	4.090000	-1.343000	0.362000	C	5.310000	-1.332000	0.373000
C	4.976000	-0.114000	0.284000	C	6.183000	-0.094000	0.306000
C	4.257000	1.217000	0.380000	C	5.447000	1.229000	0.390000
C	3.008000	1.266000	-0.532000	C	4.211000	1.264000	-0.540000
O	1.323000	0.121000	0.686000	O	2.514000	0.101000	0.647000
C	2.211000	2.549000	-0.370000	C	3.397000	2.537000	-0.391000
C	1.890000	-2.390000	-0.400000	C	3.133000	-2.406000	-0.420000
O	6.178000	-0.192000	0.152000	O	7.387000	-0.158000	0.192000
H	3.179000	-1.151000	-1.585000	H	4.424000	-1.154000	-1.588000
H	4.676000	-2.223000	0.106000	H	5.909000	-2.207000	0.125000
H	3.744000	-1.446000	1.395000	H	4.950000	-1.440000	1.401000
H	4.952000	2.017000	0.134000	H	6.136000	2.037000	0.153000
H	3.926000	1.351000	1.414000	H	5.100000	1.360000	1.419000
H	3.332000	1.168000	-1.570000	H	4.552000	1.168000	-1.573000

H	1.340000	2.548000	-1.024000	H	2.536000	2.526000	-1.056000
H	2.839000	3.399000	-0.633000	H	4.020000	3.394000	-0.647000
H	1.869000	2.668000	0.655000	H	3.041000	2.655000	0.630000
H	2.403000	-3.310000	-0.677000	H	3.661000	-3.321000	-0.689000
H	1.026000	-2.268000	-1.052000	H	2.276000	-2.295000	-1.082000
H	1.537000	-2.479000	0.624000	H	2.768000	-2.500000	0.600000
C	-3.367000	0.000000	0.032000	C	-2.338000	0.000000	0.019000
Cl	-1.613000	0.044000	0.283000	Br	-0.403000	0.035000	0.270000
Cl	-4.132000	-1.001000	1.294000	Br	-3.221000	-0.424000	1.719000
Cl	-4.030000	1.654000	0.114000	Br	-2.960000	1.752000	-0.610000
Cl	-3.729000	-0.697000	-1.571000	Br	-2.813000	-1.364000	-1.310000

Table S14. Distances and ^{13}C hyperfine coupling constants from DFT for malonate.

$d_{\text{O-H}} (\text{\AA})$	Fermi contact hyperfine constant on ^{13}C (MHz)	Energy (E_h)
2.04	0.5	-1126.51526850

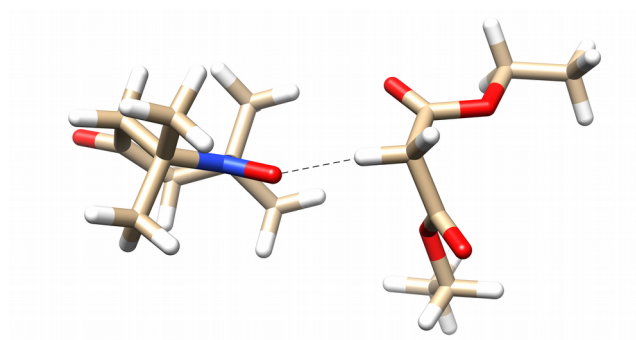


Figure S26. Geometry-optimized orientation for diethyl malonate/TN.

Table S15. Coordinates of DFT optimized geometry for diethyl malonate/TN.

1	C1	4.4393	2.2796	-0.6926	C
2	O2	3.8392	1.3587	0.3248	O
3	C3	2.4663	1.2266	0.3275	C
4	C4	2.0202	0.2811	1.4182	C
5	C5	2.6365	-1.0895	1.2533	C
6	O6	2.5769	-1.4835	-0.0722	O
7	C7	3.1362	-2.8295	-0.4110	C
8	O8	1.7289	1.8478	-0.4517	O
9	O9	3.0928	-1.8035	2.1524	O
10	C10	-4.5429	0.3467	-1.1160	C
11	C11	-3.3469	-0.4274	-1.6363	C
12	C12	-1.9948	-0.0239	-1.0049	C
13	N13	-2.1531	-0.0362	0.4979	N
14	C14	-3.4679	0.1400	1.2154	C
15	C15	-4.4349	0.9095	0.2897	C
16	O16	-5.5681	0.5123	-1.8078	O
17	O17	-1.0592	-0.2494	1.2539	O
18	C18	-4.0228	-1.2598	1.5773	C
19	C19	-3.2191	0.9564	2.4987	C
20	C20	-0.9188	-1.0554	-1.3950	C
21	C21	-1.5596	1.3927	-1.4512	C
22	H22	4.0300	3.2806	-0.5265	H
23	H23	4.1366	1.9305	-1.6842	H
24	H24	0.9300	0.1810	1.3610	H
25	H25	2.3085	0.6681	2.3994	H
26	H26	4.1769	-2.8592	-0.0746	H

27	H27	2.5631	-3.5839	0.1363	H
28	H28	-3.5320	-1.4946	-1.4397	H
29	H29	-3.2979	-0.3093	-2.7237	H
30	H30	-5.4350	0.9373	0.7348	H
31	H31	-4.0951	1.9525	0.2023	H
32	H32	-4.9304	-1.1522	2.1830	H
33	H33	-4.2699	-1.8439	0.6844	H
34	H34	-3.2715	-1.8061	2.1573	H
35	H35	-4.1769	1.1484	2.9960	H
36	H36	-2.5639	0.4088	3.1792	H
37	H37	-2.7432	1.9125	2.2563	H
38	H38	-0.8521	-1.1020	-2.4885	H
39	H39	-1.1848	-2.0468	-1.0107	H
40	H40	0.0571	-0.7781	-0.9947	H
41	H41	-2.3105	2.1471	-1.1916	H
42	H42	-1.4241	1.4040	-2.5399	H
43	H43	-0.6069	1.6549	-0.9821	H
44	C44	3.0003	-2.9671	-1.9210	C
45	H45	3.3998	-3.9367	-2.2427	H
46	H46	1.9496	-2.9047	-2.2206	H
47	H47	3.5568	-2.1742	-2.4310	H
48	C48	5.9442	2.2134	-0.4761	C
49	H49	6.3102	1.1927	-0.6235	H
50	H50	6.4498	2.8735	-1.1915	H
51	H51	6.2027	2.5341	0.5378	H

S-6 References

- (Abragam 1962) A. Abragam, *Principles of nuclear magnetism*, Oxford University Press (1962).
- (Bennati 2010) M. Bennati, C. Luchinat, G. Parigi, M.T. Türke, Water ^1H relaxation dispersion analysis on a nitroxide radical provides information on the maximal signal enhancement in Overhauser dynamic nuclear polarization experiments, *Phys. Chem. Chem. Phys.* 12 (2010) 5902–5910.
- (Buffle 2007) J. Buffle, Z. Zhang, K. Startchev, Metal flux and dynamic speciation at (bio)interfaces. Part I: critical evaluation and compilation of physicochemical parameters for complexes with simple ligands and fulvic/humic substances, *Environ. Sci. Technol.* 41 (2007) 7609–7620.
- (Denysenkov 2008) V.P. Denysenkov, M.J. Prandolini, A. Krahn, M. Gafurov, B. Endeward, T.F. Prisner, High-field DNP spectrometer for liquids, *Appl. Magn. Reson.* 34 (2008) 289–299.
- (Denysenkov 2010) V. Denysenkov, M.J. Prandolini, M. Gafurov, D. Sezer, B. Endeward, T.F. Prisner, Liquid state DNP using a 260 GHz high power gyrotron, *Phys. Chem. Chem. Phys.* 12 (2010) 5741–5751.
- (Enkin 2015) N. Enkin, G. Liu, M. del Carmen Gimenez-Lopez, K. Porfyrakis, I. Tkach, M. Bennati, A high saturation factor in Overhauser DNP with nitroxide derivatives: the role of ^{14}N nuclear spin relaxation, *Phys. Chem. Chem. Phys.* 17 (2015).
- (Gruber 1974) K. Gruber, J. Forrer, A. Schweiger, H.H. Gunthard, Computer controlled ENDOR spectrometer, *J. Phys. E.* 7 (1974) 569–574.
- (Hexem 1976) J. G. Hexem, U. Edlund, G. C. Levy, Paramagnetic relaxation reagents as a probe for translational motion of liquids, *J. Chem. Phys.* 64 (196) 936–941.
- (Kovacs 1990) H. Kovacs, J. Kowalewski, A. Laaksonen, Molecular dynamics simulation of liquid mixtures of acetonitrile and chloroform, *J. Phys Chem.* 94 (1990) 7378–7385.
- (Kucuk 2016) S.E. Küçük, D. Sezer, Multiscale computational modeling of ^{13}C DNP in liquids, *Phys. Chem. Chem. Phys.* 18 (2016) 9353–9357.
- (Liu 2017) G. Liu, M. Levien, N. Karschin, G. Parigi, C. Luchinat, M. Bennati, One-thousand-fold enhancement of high field liquid nuclear magnetic resonance signals at room temperature, *Nat. Chem.* 9 (2017) 676–680.
- (Neugebauer 2013) P. Neugebauer, J.G. Krummenacker, V.P. Denysenkov, G. Parigi, C. Luchinat, T.F. Prisner, Liquid state DNP of water at 9.2 T: an experimental access to saturation., *Phys. Chem. Chem. Phys.* 15 (2013) 6049–56.
- (Neugebauer 2014) Neugebauer, J.G. Krummenacker, V.P. Denysenkov, C. Helmling, C. Luchinat, G. Parigi, T.F. Prisner, High-field liquid state NMR hyperpolarization: a combined DNP/NMRD approach, *Phys. Chem. Chem. Phys.* 16 (2014) 18781–18787.
- (Müller-Warmuth 1968) W. Müller-Warmuth, R. van Steenwinkel, F. Noack, Dynamic nuclear polarization experiments on ^{19}F in solutions and their interpretation by the “Pulse model” of molecular collisions, *Zeitschrift Für Naturforschung A* 23 (1968) 506–513.

- (Müller-Warmuth 1976) W. Müller-Warmuth, R. Vilhjalmsson, P. a. M. Gerlof, J. Smidt, J. Trommel, Intermolecular interactions of benzene and carbon tetrachloride with selected free radicals in solution as studied by ^{13}C and ^1H dynamic nuclear polarization, *Mol. Phys.* 31 (1976) 1055–1067.
- (Parigi 2018) G. Parigi, E. Ravera, M. Bennati, C. Luchinat, Understanding Overhauser Dynamic Nuclear Polarisation through NMR relaxometry, *Mol. Phys.* (2018) DOI:10.1080/00268976.2018.1527409.
- (Polnaszek 1984) C.F. Polnaszek, R.G. Bryant, Nitroxide radical induced solvent proton relaxation: Measurement of localized translational diffusion, *J. Chem. Phys.* 81 (1984) 4038–4045.
- (Ravera 2016) E. Ravera, C. Luchinat, G. Parigi, Basic facts and perspectives of Overhauser DNP NMR, *J. Magn. Reson.* 264 (2016) 78–87.
- (Rosay 2016) M. Rosay, M. Blank, F. Engelke, Instrumentation for solid-state dynamic nuclear polarization with magic angle spinning NMR, *J. Magn. Reson.* 264 (2016) 88–98.
- (Türke 2010) M.T. Türke, I. Tkach, M. Reese, P. Hofer, M. Bennati, Optimization of dynamic nuclear polarization experiments in aqueous solution at 15 MHz/9.7 GHz: a comparative study with DNP at 140 MHz/94GHz, *Phys. Chem. Chem. Phys.* 12 (2010) 5893–5901.
- (Türke 2011) M.-T. Türke, M. Bennati, Saturation factor of nitroxide radicals in liquid DNP by pulsed ELDOR experiments, *Phys. Chem. Chem. Phys.* 13 (2011) 3630.
- (Türke 2012) M.-T. Türke, G. Parigi, C. Luchinat, M. Bennati, Overhauser DNP with ^{15}N labelled Frémy's salt at 0.35 Tesla, *Phys. Chem. Chem. Phys.* 14 (2012) 502–510.
- (Türke 2012b) M.T. Türke, M. Bennati, Comparison of Overhauser DNP at 0.34 and 3.4 T with Frémy's salt, *Appl. Magn. Reson.* 43 (2012) 129–138.
- (Weis 1999) V. Weis, M. Bennati, M. Rosay, J.A. Bryant, R.G. Griffin, High-Field DNP and ENDOR with a novel multiple-frequency resonance structure, *J. Magn. Reson.* 140 (1999) 293–299.